ST12 汽车钢板拉剪点焊接头的疲劳强度

王瑞杰[1]， 杨锡阶[2]， 肖正明[1]
(1. 昆明理工大学 机电工程学院，昆明 650500; 2. 昆明理工大学 土木工程学院，昆明 650500)

摘 要：针对车身使用的ST12低碳钢板，利用生产线上焊接设备制备了电阻点焊接头拉剪疲劳试件. 对点焊接头区域进行了金相组织观测，测量了焊点附近的维氏硬度值分布. 在MTS材料疲劳试验机上进行了恒幅疲劳加载，得到了ST12低碳钢板的电阻点焊接头的S－N曲线. 基于所得的S－N曲线进行了两级疲劳加载试验，对两级加载下的线性累积疲劳损伤进行了分析. 累积损伤结果分析表明，ST12低碳钢板电阻点焊件在两级加载下存在加载次序效应，高—低加载次序下加载次序效应更为明显.

关键词：点焊接头；疲劳寿命；两级加载；加载次序
中图分类号：TG 407 **文献标识码**：A **文章编号**：0253－360X(2014)06－0035－04

0 序 言

电阻点焊连接在疲劳破坏时，由于裂纹观测困难，且焊点常处于多轴应力状态[1]，其疲劳寿命预测始终是研究的难点. 点焊结构的疲劳寿命取决于应力水平、焊接工艺和几何结构，以及接头形式、焊接参数、母材性能、工作环境等[2-4]. 复杂加载条件下材料的疲劳损伤问题受到广泛关注.

作为复杂加载的基本形式，两级加载下的研究结果对复杂加载下的疲劳寿命研究有重要意义. 研究表明，一些材料的载荷次序效应不明显[5]，变幅加载的载荷次序对点焊结构的影响也不明显[6-8]. 而两级加载下点焊试件表现出载荷次序效应[9]，其对疲劳强度的影响有待进一步查明.

文中对点焊接头进行了恒幅和两级疲劳加载，并分析应力水平对累积损伤和疲劳寿命的影响.

1 疲劳加载试验

文中拉剪点焊试样在云南汽车厂生产线上完成焊接，结构如图1所示. 材料为ST12普通冷轧钢低碳钢板，测得弹性模量 $E = 194.4$ GPa，泊松比 $\nu = 0.33$，密度为 $\rho = 7\ 800$ kg/m^3.

1.1 点焊接头处的金相分析

将试样沿长度方向剖开，在Leica数码显微镜下观察到焊核截面如图2所示，焊核、热影响区和母材三部分界线明显，焊核直径约6.3～6.5 mm. 焊核周围组织和性能渐变的热影响区宽度约为1 mm. 焊接区域上下表面的电极压痕内凹0.1～0.2 mm.

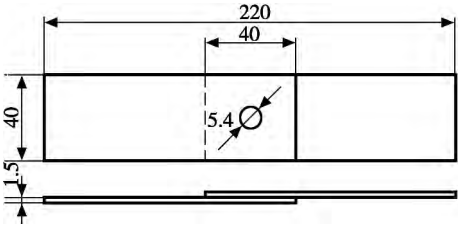

图1 点焊试样的结构(mm)
Fig. 1 Spot welds specimen

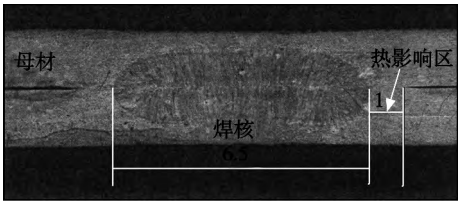

图2 焊点区域截面
Fig. 2 Spot welds cross-section

图3为Leica数码显微镜观察到的母材、热影响区和焊核三个区域的金相组织. 图3a为母材，主要为铁素体和珠光体；图3b为热影响区，主要为贝氏体和少量铁素体；图3c为焊核，主要为铁素体与贝氏体与少量马氏体. 由于马氏体和贝氏体的存在，焊点的强度大大提高.

收稿日期：2013－01－22
基金项目：国家自然科学基金资助项目(51065012)；高等学校博士学科点专项科研基金资助课题(20105314120013)；昆明理工大学分析测试基金资助项目(2010313)

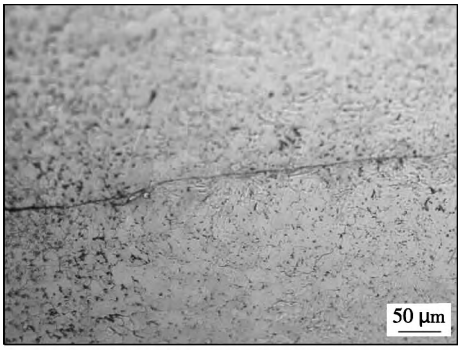

(a) 母材区

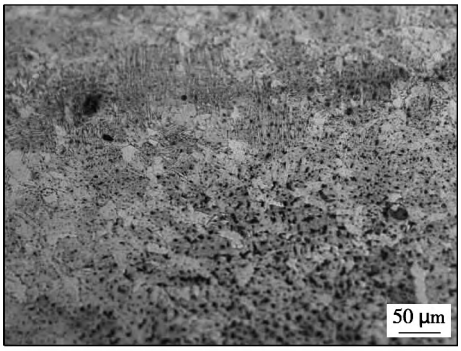

(b) 热影响区

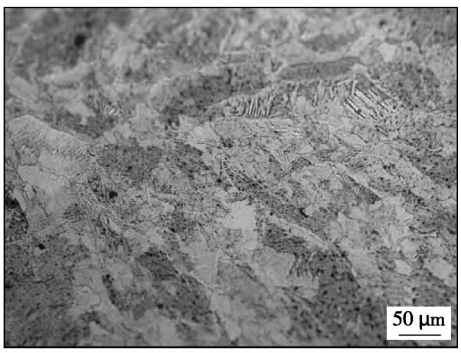

(c) 焊核区

图 3 点焊接头金相组织

Fig. 3 Microstructure in spot welded joints

测量焊核处的维氏硬度如图 4 所示，图 4 中为距两板结合面的不同远近三排测量点处的硬度值. 在焊点周围热影响区，从母材到焊核的硬度值呈非线性增加；在板厚方向，接近板的内侧面处硬度值较高. 焊核及热影响区的硬度都比母材要高. 由于硬度与强度间存在近似正比关系[10]，可以看出焊核的强度最高，热影响区次之，母材的强度最低.

1.2 恒幅加载疲劳试验

疲劳试验均使用 MTS810-100KN 电液伺服材料试验机，加载频率为 10 ~ 15 Hz，控制应力加载，载荷波形为三角波，试验均在室温空气中进行. 试样完全破坏时的加载循环数记为全疲劳寿命.

以疲劳寿命 N_f 为横坐标，名义应力幅 $\Delta\sigma_a$ 为纵坐标，绘制 $\Delta\sigma_a - N_f$ 关系如图 5 所示. 此处名义应力为外载与板横截面积的比值. 在双对数坐标下，应力幅与疲劳寿命呈现近似线性的关系. 将此关系拟合成一条直线，给出方程为

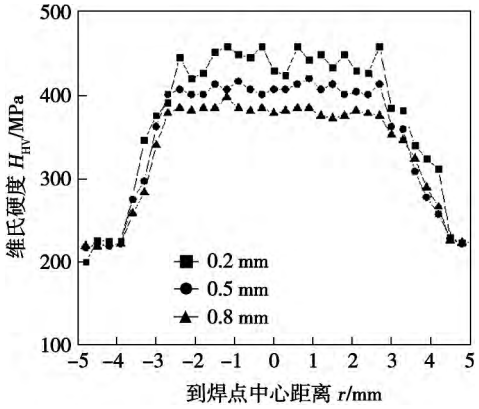

图 4 焊核处的维氏硬度

Fig. 4 Vickers hardness around weld nugget

$$\Delta\sigma^{4.1288} N_f = 10^{10.7996} \quad (1)$$

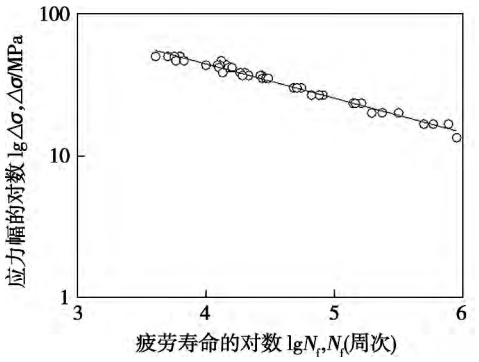

图 5 应力幅与疲劳寿命

Fig. 5 Load amplitude vs. fatigue life

1.3 两级加载疲劳试验

依据恒幅疲劳试验结果式(1)，所选取的两级应力水平如表 1 所示. 低—高加载时，先在低应力水平下加载到预定的循环数，然后在高应力水平下加载，直到试样最终破坏；高—低加载时，先在高应

表 1 两级加载的应力水平

Table 1 Loadings for two-level loading test

组号	应力水平	平均应力 σ_m/MPa	应力幅 σ_a/MPa	疲劳寿命 N_f(周次)
A	水平一	60	35.00	29 206
	水平二	60	50.00	5 481
B	水平一	60	23.33	149 737
	水平二	60	35.00	29 206
C	水平一	60	23.33	149 737
	水平二	60	50.00	5 481

力水平下加载，再在低应力水平下加载.

两级加载疲劳试验结果如表 2、表 3 所示. 每个载荷水平下有 1 ~ 2 个试件. 第一个应力水平下的循环数记为 n_1，第二级应力下的疲劳寿命，即剩余寿命记为 n_{e2}. 两表中 n_1/N_1 为第一个应力水平作用到的循环比，n_2 为使用 Miner 线性疲劳累积损伤法则估算的剩余寿命.

表 2　低—高加载的疲劳寿命

Table 2　Fatigue test results under low-high loading

组别	一级循环数 n_1(周次)	一级循环比 n_1/N_1	预测剩余寿命 n_2(周次)	试验剩余寿命 n_{e2}(周次)	
A	4 000	0.14	4 714	6 237	5 528
A	8 000	0.27	4 001	3 965	4 904
A	12 000	0.41	3 234	5 720	3 473
A	16 000	0.55	2 466	5 012	3 895
A	20 000	0.68	1 754	3 382	1 371
A	24 000	0.82	987	1 616	2 464
B	25 000	0.17	24 241	20 580	22 464
B	50 000	0.33	19 568	13 564	12 726
B	75 000	0.50	14 603	12 774	10 973
B	100 000	0.67	9 638	4 900	4 105
B	125 000	0.83	4 965	1 130	—
C	25 000	0.17	4 566	8 709	5 293
C	50 000	0.33	3 651	6 028	4 613
C	75 000	0.50	2 736	4 319	4 744
C	100 000	0.67	1 821	2 855	7 410
C	125 000	0.83	905	2 030	—

由表 2 可以看出，低—高加载时，A 组剩余寿命大于按 Miner 线性疲劳累积损伤法则所预测的剩余寿命. 而 B 组剩余寿命均小于按 Miner 法则预测的剩余寿命. A 组剩余寿命大于按 Miner 法则所预测的剩余寿命. 在表 3 中，对于高—低加载，A，B，C 3 组试验结果中，除一个试样以外，其它试样的剩余寿命均明显大于使用 Miner 法则所预测的剩余寿命，甚至出现了剩余寿命大于第二级应力单独作用时的全疲劳寿命的情况，如 C 组中全部 5 个试样.

2　两级加载下的线性累积损伤

使用 Miner 线性疲劳累积损伤法则，计算表 2 与表 3 前后两次加载的循环比，得到累积疲劳损伤 $D = \Sigma n_i/N_i$. 此处 N_i 为第 i 个应力水平下的疲劳寿命. 线性累积损伤值随第一级应力循环比 n_1/N_1 的变化分别如图 6 与图 7 所示. 两图中累积损伤均有这样的规律：随着小应力水平下的载荷循环数增加，疲劳损伤累积值增加；而随着大应力水平载荷循环数的增加，疲劳损伤累积值减小. 显然，由疲劳损伤累积理论可知，此处疲劳寿命取决于加载的次序.

表 3　高—低加载的疲劳寿命

Table 3　Fatigue test results under high-low loading

组别	一级循环数 n_1(周次)	一级循环比 n_1/N_1	预测剩余寿命 n_2(周次)	试验剩余寿命 n_{e2}(周次)	
A	1 000	0.18	23 877	23 643	38 301
A	2 000	0.36	18 549	12 765	25 630
A	3 000	0.55	13 220	10 173	12 337
A	4 000	0.73	7 892	26 714	19 212
B	5 000	0.17	124 102	212 159	285 515
B	10 000	0.34	98 468	117 630	176 165
B	15 000	0.51	72 833	87 000	75 976
B	20 000	0.68	47 198	92 637	45 575
B	25 000	0.86	21 564	35 281	17 081
C	1 000	0.18	122 418	186 767	413 691
C	2 000	0.36	95 098	263 248	448 540
C	3 000	0.55	67 779	212 474	195 526
C	4 000	0.73	40 460	195 719	290 014
C	5 000	0.91	13 141	212 541	200 647

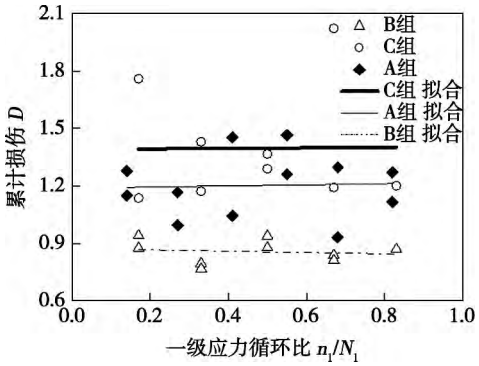

图 6　低—高加载下线性累积损伤

Fig. 6　Linearly cumulated damage under low-high loading

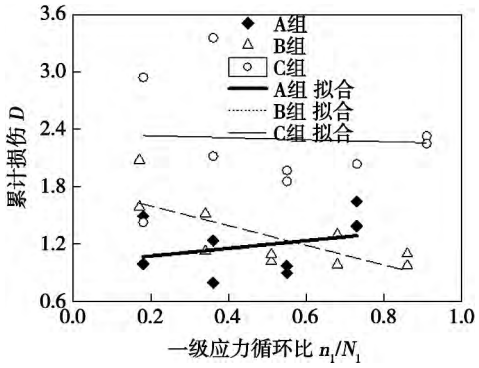

图 7　高—低加载下线性累积损伤与一级应力循环比

Fig. 7　Linearly cumulated damage under high-low loading

由图 6 可见，A 组与 C 组的累积损伤均大于 1，而 B 组的累积损伤均小于 1. 由疲劳累积损伤理论可知，低—高加载时，受由低到高的加载次序的影响，线性损伤累积法则得到的累积损伤呈现大于 1

的趋势. A 组与 C 组与此趋势基本符合,表现出一定的"锻炼效应". 而 B 组中,未表现出低—高加载的"锻炼效应",但是从数值来看,均小于 1,表明累积损伤呈现一定的规律,体现出一定加载次序效应.

由此可见,对于点焊试样,在低—高加载的情况下,加载次序对累积损伤有明显的影响. 综合 3 组结果看来,随着低应力水平加载循环数的增多,累积损伤值的变化趋势并不明显.

由图 7 可见,高—低加载时,受由高到低加载次序的影响,累积损伤值也呈现出大于 1 的趋势. 由线性累积损伤理论可知,对于钢制缺口件,高低加载时,会出现累积损伤大于 1 的情况. 由此可见,此处的损伤累积结果体现了点焊连接的缺口特点.

高—低加载时,应力次序对疲劳累积损伤也有明显影响. A 组的累积损伤中,随着大应力水平循环数的增加,线性疲劳损伤累积值有增加的趋势. B 组与 C 组中,随大应力水平循环数的增加,损伤累积值有减小的趋势,B 组减小趋势较明显,C 组的变化不明显. 但 3 组总起来看,累积损伤的变化规律并不清晰. C 组由于剩余寿命均大于由线性累积损伤法则估计的剩余寿命,因而累积损伤均大于 1.

由以上分析可知,加载次序对于 ST12 钢拉剪点焊试样的疲劳累积损伤有明显的影响. 点焊连接在两级加载下体现出了缺口件的累积损伤特点.

3 试验结果讨论

由表 1 可见,A 组的应力水平最高,两个应力水平中一个属于低周,另一个为低高周过渡区; B 组的应力水平最低,水平一为高周,水平二为 A 组中的水平一; C 组的两个应力水平分别位于高低周.

由累积损伤理论可知,低—高加载时,无论光滑件还是缺口件,破坏时线性累积损伤一般均大于 1. 高—低加载时,钢制缺口件有两种情况: 合金钢累积损伤小于 1,低碳钢累积损伤均值大于 1; 钢制光滑件累积损伤一般常小于 1. 此处低—高次序加载时,A 与 C 两组的累积损伤出现了较明显的"锻炼效应",但 B 组累积损伤却出现了小于 1 的情形. 可以看出存在应力次序效应,但不够明显.

高—低加载下,在高平均应力和大应力幅作用一段时间后,出现剩余寿命均大于按线性累积损伤理论所计算的剩余损伤所对应的剩余寿命的趋势. 甚至出现了剩余寿命大于低应力单独作用下全疲劳寿命的情况. 由图 7 可见,A,B,C 三组损伤数值均大于 1,体现出明显的缺口效应. C 组与另外两组对比可见,应力水平相差大时,缺口效应越明显.

因而由上述损伤累积规律可知,ST12 钢点焊件高—低与低—高加载时,体现出缺口效应.

4 结 论

(1) ST12 钢拉剪点焊件高—低与低—高加载时,均体现出了缺口效应.

(2) ST12 钢拉剪点焊试样在高—低两级疲劳加载下,当应力水平在一定范围内时,剩余寿命会大于低应力单独作用下的全寿命.

参考文献:

[1] 薛 河. 点焊结构应力应变场数值模拟分析 [J]. 汽车技术, 2002, 10: 33 - 35.
Xue He. Numerical simulating analysis of stress and strain field of spot welding structure [J]. Automible Technology, 2002, 10: 33 - 35.

[2] Sheppard S D, Strange M. Fatigue life estimation in resistant spot welds: initiation and early growth phase [J]. Fatigue & Fracture of Engineering Materials & Structure, 1992, 15(6): 531 - 549.

[3] Zhang Y, Taylor D. Sheet thickness effect of spot welds based on crack propagation [J]. Engineering Fracture Mechanics, 2000, 67(1): 55 - 63.

[4] Rathbun R W, Matlock D K, Speer J G. Fatigue behavior of spot welded high-strength sheet steels [J]. Welding Journal, 2003, 82(8): 207s - 218s.

[5] Richard A, Everett Jr. The effects of load sequencing on the fatigue life of 2024-T3 aluminum alloy [J]. International Journal of Fatigue, 1997, 19(93): 289 - 293.

[6] 臧启山, 袁金才. 点焊接头在复杂载荷谱下的疲劳研究 [J]. 焊接学报, 1989, 10(4): 265 - 270.
Zang Qishan, Yuan Jincai. Fatigue behaviour of spot welded joints under complex spectrum loading [J]. Transactions of the China Welding Institution, 1989, 10(4): 265 - 270.

[7] Wang Ruijie, Shang Deguang. Fatigue life prediction based on natural frequency changes for spot welds under random loading [J]. International Journal of Fatigue, 2009, 31(2): 361 - 366.

[8] 王瑞杰, 尚德广. 变幅载荷作用下的拉剪点焊结构的疲劳强度研究 [J]. 焊接学报, 2007, 28(9): 1 - 4.
Wang Ruijie, Shang Deguang. Fatigue damage of spot welding under variable amplitude load [J]. Transactions of the China Welding Institution, 2007, 28(9): 1 - 4.

[9] 王瑞杰, 尚德广, 刘泓滨. 两级加载下两点拉剪点焊接头的损伤 [J]. 焊接学报, 2010, 31(12): 77 - 80.
Wang Ruijie, Shang Deguang, Liu Hongbin. Damage of two-spot welds under two level loading [J]. Transactions of the China Welding Institution, 2010, 31(12): 77 - 80.

[10] Lee K S, Song J H. Estimation methods for strain-life fatigue properties from hardness [J]. International Journal of Fatigue, 2006, 28(4): 386 - 400.

作者简介: 王瑞杰,男,1972 年出生,博士,副教授,硕士研究生导师. 主要从事机械结构强度及现代机械设计理论与方法方面的研究. 发表论文 30 余篇. Email: wrj@kmust.edu.cn

China; 2. Department of Mechanical Engineering, Tsinghua University, Beijing 100084, China). pp 17 – 20

Abstract: Single-pass tungsten inert welding with TGS-56 filling wire was conducted on 100 mm thick SA508-III steel used for nuclear pressure vessel and the macrostructure of the cross section of the welded joints was examined to analyze the effect of different welding parameters on the geometry of the welded joint. The results show that d changed obviously with the welding current, the wire feed speed mainly affected the bead height and the welding speed had great effect on the welded joint geometry. Temper bead welding technology could be easily achieved by using smaller welding current and greater wire feed speed to make $b + h$ larger than d. The difference between $b + h$ and d did not vary significantly with the welding speed.

Key words: temper bead welding technology; welded joint geometry; welding current; wire feed speed; welding speed

Pores distribution during laser-cladding NiCuFeBSi alloy on gray cast iron YAN Shixing, DONG Shiyun, XU Binshi, WANG Yujiang, FANG Jinxiang, REN Weibin (National Key Laboratory for Remanufacturing, Academy of Armored Forces Engineering, Beijing 100072, China). pp 21 – 25

Abstract: With contrast of different kinds of pores characterization in cladding layers fabricated on the substrates of 45 steel and HT250, the composition, distribution and influence factors were investigated, respectively. The results show that the gas in pore was CO which was generated by the reaction of graphite and oxide. The shape of pores was irregular with many wedge angles. Furthermore, the floating path of pores was disperse instead of vertical due to the severe convection in molten pool. And the spread acceleration of pores was increased with the temperature as well as the surface tension gradient in the molten pool. However, the laser cladding parameters were the external factors affecting the distribution of pores. Enhancing the preheat temperature and reducing the laser power and laser scanning speed appropriately could avoid the generation of pores and decrease the porosity in the cladding layer.

Key words: laser cladding; gray cast iron; pore; convection

Effect of processing parameters on electron temperature of vacuum arc with hollow cathode XU Jianping[1,2], GONG Chunzhi[1], TIAN Xiubo[1], YANG Shiqin[1] (1. State Key Laboratory of Advanced Welding and Joining, Harbin Institute of Technology, Harbin 150001, China; 2. Department of Materials and Chemical Engineering, Heilongjiang Institute of Technology, Harbin 150050, China). pp 26 – 30

Abstract: The spectral distribution of hollow cathode vacuum arc was acquired using spectrometer with different processing parameters, and the electronic excitation temperature of the arc plasma was calculated by the method of relative intensity. The results show that the hollow cathode vacuum arc plasma was composed of argon ions and argon atoms. The ion concentration in hollow cathode vacuum arc gradually increased with reducing the discharge pressure and increasing the welding current. At a certain gas flow, the electron excitation temperature in the hollow cathode vacuum arc gradually increased as the welding current increased. It is also found that the electron excited temperature was higher at lower gas flow and large welding current. If the discharge pressure became larger, the vacuum arc hollow cathode electron excitation temperature might decrease. With larger welding current and relatively lower gas flow rate, the argon ion spectrum intensity was high around the center axis of the hollow cathode arc. This was beneficial for welding with larger penetration.

Key words: hollow cathode; vacuum arc; emission spectrometer; electron temperature

Pulse current auxiliary liquid diffusion bonding between Ti(C, N)-Al_2O_3 CMC and 40Cr steel WU Mingfang, WANG Fei, WANG Fengjiang, XU Guoxiang (Provincial Key Laboratory of Advanced Welding Technology, Jiangsu University of Science and Technology, Zhenjiang 212003, China). pp 31 – 34

Abstract: Diffusion bonding behavior between Ti(C, N)-Al_2O_3 ceramic matrix composites (CMC) and 40Cr steel was investigated using pulse current auxiliary liquid diffusion bonding process. The effect of aided pulse current and holding time during diffusion bonding on the element distribution, phase structure and thickness of the reactive layer at the interface was characterized. The results show that aided pulse current during diffusion bonding promoted the metallurgical bonding between CMC and 40Cr steel. The corresponding joint strength was about 146 ~ 180 MPa and was not obviously affected by the holding time during bonding. The diffusion path and rate of atoms at the interface were apparently changed by the loading of pulse current during diffusion bonding. Consequently, the growth of interfacial intermetallic compounds and the content of low melting point eutectic phases could be controlled to improve the joint strength.

Key words: Ti(C, N)-Al_2O_3; liquid diffusion bonding; aided pulse current; interfacial structure; joint strength

Fatigue strength of tensile shear spot welds made of ST12 steel WANG Ruijie[1], YANG Xijie[2], XIAO Zhengming[1] (1. Mechanical Engineering Faculty, Kunming University of Science and Technology, Kunming 650500, China; 2. Civil Engineering Faculty, Kunming University of Science and Technology, Kunming 650500, China). pp 35 – 38

Abstract: Fatigue specimens were made of ST12 steel sheets with product line welding equipment. Microstructure in different zones was observed and Vicker's hardness around the weld nugget was measured. Constant amplitude fatigue loading was applied on specimens with MTS material testing frame to obtain the S-N curve. According to the constant amplitude fatigue test results, two-stage loading tests were carried out, and then

linear damage accumulation rule was used for damage analysis under two-stage loading. Damage accumulation results show that there was loading sequence effect for low carbon ST12 steel spot welded joint under two-stage loading, the loading sequence effect under high-low loading sequence was even more explicit.

Key words: spot weld; fatigue life; two-stage loading; loading sequence

Probability-sorting based inspection method for chip type solder joints WU Fupei[1], LI Shengping[1], ZHANG Xianmin[2] (1. Department of Mechatronic Engineering, Shantou University, Shantou 515063, China; 2. School of Mechanical and Automotive Engineering, South China University of Technology, Guangzhou 510640, China). pp 39 - 43

Abstract: A probability-sorting based inspection method was proposed for chip type solder joints to improve the performance of automatic optical inspection on classification of solder joint, inspection accuracy and inspection speed. The algorithm of solder joint inspection was designed by analyzing the colorful images of solder joints, establishing model for each solder joint, defining inspection zone, extracting area of region, center of gravity and color gradient characters, and planning the inspection sequence. The experimental results illustrate that the proposed method could effectively detect and classify eight common types of chip solder joints with high inspection rate, which is useful for quality control in manufacturing process. And the inspection speed was obviously faster than other methods, which was helpful to improve the efficiency of manufacturing process.

Key words: automatic optical inspection; solder joint inspection; chip; color grads

Effect of Cr and Mo contents on corrosion resistance and mechanical properties of weathering steel deposited metal XIAO Xiaoming, PENG Yun, TIAN Zhiling (State Key Laboratory of Advanced Steel Processes and Products, Central Iron & Steel Research Institute, Beijing 100081, China). pp 44 - 48

Abstract: The effect of Cr and Mo content on corrosion resistance and mechanical properties of weathering steel deposited metal was investigated by cycle immersion corrosion test, rust layer micro-analysis and electrochemical test. The experimental results indicate that corrosion resistance of deposited metal was improved with the increase of Cr and Mo contents. Mo improved the corrosion resistance better than Cr. Cr and Mo enriched in the rust layer as Cr_2O_3, $FexCr_{3-x}O_4$, $MnFexCr_{2-x}O_4$, $Mn_{1-x}FexCr_2O_4$, $NiFe_xCr_{2-x}O_4$ and MoO_3, which promoted the compactness of rust layer, impeded the anode dissolution and enhanced the protecting performance of rust, so the corrosion resistance of deposited metal was improved. With the increase of Cr and Mo contents, the strength of deposited metal also improved, whereas the impact toughness declined sharply. At the same time, the contents of M-A constituent and granular bainite increased while the acicular ferrite decreased. The change of microstructure was the main reason for increase of strength and deterioration of toughness.

Key words: weathering steel; deposited metal; corrosion resistance; mechanical property

Diffusion and dissolve mechanism of Al/Ti diffusion layer formation SONG Yuqiang, MA Shengdong, LI Shichun (Liberation Army Chief Equipment Ministry Laboratory of Material Interface, China University of Petroleum, Qingdao 266580, China). pp 49 - 52, 89

Abstract: Al/Ti diffusion couple made by inlaying was annealed under and above Al melting point, respectively, and solid-solid and solid-liquid diffusion couples were formed. The microstructure of Al/Ti solid-solid and solid-liquid diffusion layers were observed by OM and SEM-EDS, and the formation mechanism was investigated. The results show that Al/Ti solid-solid diffusion layer was composed by one layer of $TiAl_3$. But the solid-liquid diffusion layer was composed of single phase layer of $TiAl_3$ and dual-phase layer of $TiAl_3$ + Al (Ti) solid solution. The formation of dual-phase layer changed regularly from Al to Ti. The Al/Ti solid-solid $TiAl_3$ diffusion layer and solid-liquid single-phase $TiAl_3$ layer were formed from diffusion of Al into Ti by forming Al-Ti solid solution with Ti as solvent. However, dual-phase layer $TiAl_3$ + Al(Ti) solid solution formed by dissolving and spread of Ti to the liquid Al by forming Al-Ti liquid solution. It resulted in morphological variation of dual-phase layer $TiAl_3$ + Al(Ti) solid solution that Ti atom concentration gradually increased in Al solution from Al to Ti.

Key words: diffusion layer; diffusion welding; diffusion; dissolve; crystal

Mathematical model and RP simulation of opening and welding mating surface of two intersecting pipes HUANG Shiyou, XU Lei, REN Qingchuan, YE Zhenzhen (School of Manufacturing Science & Engineering, Sichuan University, Chengdu 610065, China). pp 53 - 56

Abstract: To achieve the cutting of opening and welding mating surface in two intersecting pipes by five-axis linkage CNC machine, this paper introduced a mathematical model about irregular saddle shape hole based on analytic geometry and principle of numerical integration after analyzing interpenetrating model of eccentric pipes. A model of welding mating surface with blunt edge was established based on the riding type and insertion type of lap welding. This paper analyzed the processing methods and the accuracy of CNC machine based on the model. Related data were generated by AutoCAD VBA programming. By comparing with the physical models produced by rapid prototyping (RP) technology, the result verifies the reliability and generality of mathematical models for the opening and welding mating surface and the accurate control method. It also illustrates the RP technology had many advantages in simulating and lapping of circular pipes.